Hindawi
Mathematical Problems in Engineering
Volume 2019, Article ID 6316538, 12 pages
https://doi.org/10.1155/2019/6316538

Research Article

A Novel Engagement-Pixel Tracking Method for Meshing Clearance Layout of Twin-Screw Rotors

Jie Lu, Zhiqin Cai, Sijie Cai, Bin Yao, and Binqiang Chen

School of Aerospace Engineering, Xiamen University, Xiamen 361005, China

Correspondence should be addressed to Zhiqin Cai; caizhiqin@xmu.edu.cn and Bin Yao; yaobin@xmu.edu.cn

Received 29 May 2019; Revised 2 August 2019; Accepted 19 August 2019; Published 22 September 2019

Academic Editor: Eric Feulvarch

The performance of dry twin-screw compressors is primarily affected by the meshing clearance between a pair of meshing rotors. In this paper, a novel method for meshing clearance layout (MCL) is presented. The presented method is based on the engagement-pixel tracking (EPT) technique, which utilizes discrete-pixel curves generated by the two rotors. An algorithm for the proposed method is put forward. Firstly, when the profile of one rotor is known, the discrete point coordinates of the two rotor profiles and their thermal expansion profiles can be obtained. Secondly, the instantaneous contact models of the two rotors at special meshing positions are acquired under pixel coordinate system. Thirdly, through inspecting the pixels on the profile of a rotor and establishing the corresponding normal vector, the meshing clearance of the two rotors is extracted. Then, the meshing clearances can be generated by extracting the boundary pixels on the other rotor profile. Finally, the meshing clearance layout method is proposed. To verify the effectiveness of the presented method, a case study was conducted on a pair of meshing rotors to extract its meshing clearance. It was shown that the proposed method can be used as a tool for evaluating the clearance distribution of actual machined profiles.

1. Introduction

Screw rotors are the core component of screw compressors. Meshing clearance between screw rotors, either due to manufacturing error, assembly misalignment, or thermal expansion during working process, can lead to leakage and decreased efficiency of the compressor. In a twin-screw compressor, a proper working clearance must be guaranteed because a large clearance can also cause a side effect for excessive leakage [1–4].

At present, in order to improve the performance of rotary compressors, one of the major research trends is to optimize the theoretical and actual rotor profiles [5–8]. For the purpose of optimization, working clearances need to be arranged. Because of the high-pressure fluid in the shell of screw compressor, thermal expansion is caused with the rise of temperature at the discharge end, leading to potential interference and abrasion between the intermeshing rotor surfaces and the existence of various leakage paths. In terms of the design of rotor clearance, methods for calculating the initial clearances between meshing conjugate teeth, including the profile correction method, center distance adjustment method, machining correction method, and mixed method, were described by Xing [9]. A method to analyze clearance distribution between rotors with theoretical, modified design, and machined profiles was developed by Huang et al. [10]. A mathematical model of rotor transmission, which can predict the actual rotor positions, reducing rotor profile clearances and improving screw compressor characteristics, was proposed by Mustafin et al. [11]. A numerical method for evaluating meshing clearance of screw rotors was proposed by Wu and Chi [12]. By using this method, the clearance between the two screw rotors can be attained and eliminated. A novel localization algorithm for meshing simulation and clearance evaluation was proposed by Jiing et al. [13]. This method can be used to determine the initial contact position of the screw rotor pair and compute the clearance distribution diagram along the sealing line. A case study of an oil-injected compressor tested at elevated discharge temperatures with original and revised

clearances was investigated by Buckney et al. [14, 15]. The nature of the contact between the load transferring surfaces in the screw mechanism was investigated by Jones and Velinsky [16] and Fu et al. [17], which was necessary for the calculation of the contact positions and clearances between helical surfaces.

In this study, the discrete points of a female rotor profile, measured from 2D coordinate measuring system, are used to conduct the meshing clearance layout. To generate intermeshing profiles of the male and female rotors, the measured data points of the rotor profile are employed by using the enveloping equation. Furthermore, combining the engagement theory and pixel-tracking technique in computer graphics, a novel engagement-pixel tracking (EPT) method for meshing clearance calculation is presented. The corresponding meshing layout method is proposed. To verify the effectiveness of the presented method, a case study is conducted on a pair of rotors to extract its meshing clearance.

2. Generation Method of Intermeshing Rotor Profiles and Contact Line

In this paper, the 2D coordinate measuring point data from the end-section profile of a female rotor are used as the input for meshing clearance calculation. Therefore, the meshing profiles and the contact line for a pair of meshing rotors must be performed first. Based on the meshing equation, dichotomy is used to fit the discrete points on the contact line such that the male rotor profile can be obtained.

The relative motion coordinate systems for a pair of meshing rotors are shown in Figure 1, where $S_1'(o_1' - x_1'y_1'z_1')$ and $S_2'(o_2' - x_2'y_2'z_2')$ represent the fixed coordinate systems of the male rotor and the female rotor, respectively. S_2 $(o_2 - x_2y_2z_2)$ and S_1 $(o_1 - x_1y_1z_1)$ represent the corresponding rotation coordinate systems, with the rotation angles φ_2 and φ_1, respectively. The shortest distance between the two rotary axes (z_2-axis and z_1-axis) is the center distance a.

In the coordinate system S_1, based on the discrete points $\mathbf{r}_1' = (x_1'(u), y_1'(u))$ of end-section profile and the unit normal vectors $\mathbf{n}_{1i}$ of the female rotor, the helicoid equation, $\mathbf{r}_1$ can be determined as follows:

$$\begin{aligned}\mathbf{r}_1(u,\theta) &= [x_1, y_1, z_1] = [x_1'(u)\cos(\theta) - y_1'(u)\sin(\theta),\\ &\quad y_1'(u)\cos(\theta) + x_1'(u)\sin(\theta), p\theta],\end{aligned} \tag{1}$$

$$\begin{aligned}\mathbf{n}_{1i}(u,\theta) &= \frac{\mathbf{N}_{1i}(u,\theta)}{\sqrt{\mathbf{N}_{1i}(u,\theta)\cdot\mathbf{N}_{1i}(u,\theta)}}\\ &= \left[p\frac{\partial y_1}{\partial u}, -p\frac{\partial x_1}{\partial u}, x_1\frac{\partial x_1}{\partial u} + y_1\frac{\partial y_1}{\partial u}\right];\\ \mathbf{N}_{1i}(u,\theta) &= \frac{\partial \mathbf{r}_1(u,\theta)}{\partial u}, \quad i = x, y, z,\end{aligned} \tag{2}$$

where p and θ are the helix parameters and u is accumulated chord length parameter.

The relative velocity between two conjugate rotor curves in the coordinate system S is as follows:

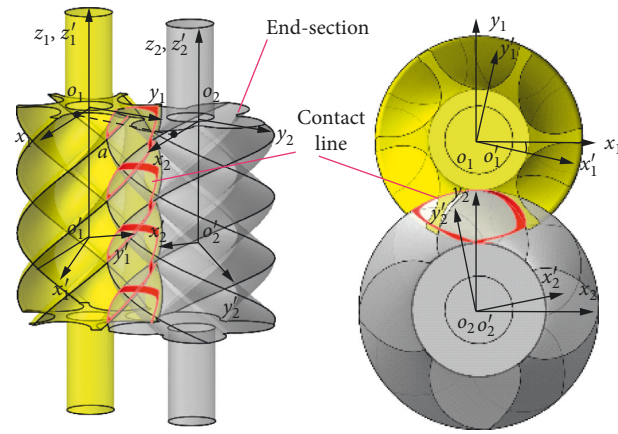

Figure 1: Coordinate systems for the male and female rotors.

$$\mathbf{v}_{12,i}(u,\varphi_1,\theta) = [-ky_1 + a\sin\varphi_1, kx_1 - a\cos\varphi_1, 0], \tag{3}$$

where $k = w - 1$ and w is the transmission ratio of twin-screw rotors.

To determine the relational expression between the parameter u and the rotational angle φ_1, the enveloping condition is that the common normal vector at the contact point is perpendicular to the relative velocity direction between the two conjugate rotor curves:

$$f(u,\varphi_1,\theta) = \mathbf{n}_{1i}(u,\theta)\cdot\mathbf{v}_{12,i}(u,\varphi_1,\theta) = 0, \quad i = x, y, z. \tag{4}$$

Substituting equations (2) and (3) in (4), the enveloping equation can be expressed as

$$(-ky_1 + a\sin\varphi_1)p\frac{\partial y_1}{\partial u} - (kx_1 - a\cos\varphi_1)p\frac{\partial x_1}{\partial u} = 0. \tag{5}$$

According to equation (5), when the helix parameter θ, evaluated from 0° to 360°, of each end-section profile is known, the corresponding contact line point coordinates $\mathbf{r}_c = (x_c, y_c, z_c)$ can be obtained by substituting the rotational angle φ_1 into equation (5) yielding the corresponding value u.

The male rotor profile equation $\mathbf{r}_1'$ and its corresponding rotation angle φ_2 can be obtained by using the coordinate transformation matrix $\mathbf{M}_{21}$ and the enveloping condition equation (5):

$$\mathbf{r}_2(u,\varphi_1) = \mathbf{M}_{21}(\varphi_1)\cdot\mathbf{r}_1'(u), \tag{6}$$

where

$$\begin{aligned}\mathbf{M}_{21}(\varphi) &= \begin{bmatrix}\cos\varphi_1 & \sin\varphi_1 & 0\\ -\sin\varphi_1 & \cos\varphi_1 & 0\\ 0 & 0 & 1\end{bmatrix}\cdot\begin{bmatrix}\cos\varphi_2 & \sin\varphi_2 & a\\ -\sin\varphi_2 & \cos\varphi_2 & 0\\ 0 & 0 & 1\end{bmatrix};\\ \varphi_2 &= w\times\varphi_1.\end{aligned} \tag{7}$$

To improve accuracy, the discrete points on the contact line are fitted by dichotomy. The method is based on piecewise cubic spline interpolation between the two adjacent points on the discrete profile. As shown in equation (6),

when the precision is set, the last interpolation point is taken as the contact line component point by repeating interpolation.

$$
\begin{aligned}
y_c^{(j)} &= \left[\frac{3}{h_{1,j}^2}\left(x_{1,j+1}-u\right)^2-\frac{2}{h_j^3}\left(x_{1,j+1}-u\right)^3\right]y_{1,j}\\
&\quad+\left[\frac{3}{h_{1,j}^2}\left(u-x_{1,j}\right)^2-\frac{2}{h_{1,j}^3}\left(u-x_{1,j}\right)^3\right]\\
&\quad+h_{1,j}\left[\frac{1}{h_{1,j}^2}\left(x_{1,j+1}-u\right)^2-\frac{1}{h_{1,j}^3}\left(x_{1,j+1}-u\right)^3\right]y'_{1,j}\\
&\quad-h_{1,j}\left[\frac{1}{h_{1,j}^2}\left(u-x_{1,j}\right)^2-\frac{1}{h_{1,j}^3}\left(u-x_{1,j}\right)^3\right]y'_{1,j+1},\\
y_c^{(j)'} &= \frac{6}{h_{1,j}}\left[\frac{1}{h_{1,j}^2}\left(x_{1,j+1}-u\right)^2-\frac{1}{h_{1,j}}\left(x_{1,j+1}-u\right)\right]y_{1,j}\\
&\quad-\frac{6}{h_{1,j}}\left(\frac{1}{h_{1,j}^2}\left(u-x_{1,j}\right)^2-\frac{1}{h_{1,j}}\left(u-x_{1,j}\right)\right)\\
&\quad+\left[\frac{3}{h_{1,j}^2}\left(x_{1,j+1}-u\right)^2-\frac{2}{h_{1,j}}\left(x_{1,j+1}-u\right)\right]y'_{1,j}\\
&\quad+\left[\frac{1}{h_{1,j}^2}\left(u-x_{1,j}\right)^2-\frac{1}{h_{1,j}^3}\left(u-x_{1,j}\right)^3\right]y'_{1,j+1},\\
&\qquad h_{1,j}=x_{1,j+1}-x_{1,j},\quad j=1,2,3\ldots.
\end{aligned}
\tag{8}
$$

By multiplying the normal vector at each point-j of the contact line $\mathbf{n}_{1i}^{(j)}$ $(i=x,y,z)$, with the normal clearance value $\delta_n^{(j)}$, the equation of the clearance distribution curve on the 3D contact line can be obtained as

$$
\begin{aligned}
\mathbf{r}_{c'}^{(j)} &= \left[x_{c'}^{(j)}, y_{c'}^{(j)}, z_{c'}^{(j)}\right]\\
&= \left[x_c^{(j)}+n_{1x}^{(j)}\delta_n^{(j)}, y_c^{(j)}+n_{1y}^{(j)}\delta_n^{(j)}, z_c^{(j)}+n_{1z}^{(j)}\delta_n^{(j)}\right],\\
&\qquad j=1,2,\ldots.
\end{aligned}
\tag{9}
$$

3. The Meshing Clearance Calculation Method

3.1. Relationship between Radial Clearance and Normal Clearance of End-Section Profile. According to the meshing theory, the best practice for clearance design is to ensure that only rolling contact exists at the pitch radius of each rotor. To achieve this, the minimum clearance is generally arranged at the pitch circle, and the larger clearance is arranged at the tooth top of the rotor. Furthermore, to arrange the required clearance on the contact line, it is necessary to adjust the corresponding point coordinates of the rotor profile.

When the lead of the screw rotor remains unchanged, as shown in Figure 2(a), the meshing clearance at the intersection point A' (between helix L and any contact line) is the same as that at the intersection point A (between helix L and end-section profile). Therefore, it is only necessary to find the corresponding point of each contact point at the end-section profile and the clearance layout effect at the point A of end-section profile is the same as that at thepoint-A' at the 3D contact line. Furthermore, as shown in Figure 2(b), the normal clearance value of 3D contact line can be obtained by projecting the meshing clearance of the end-section (d-d section) onto the normal section (n-n section), as shown in the following equation:

$$
\delta_{n'}^{(j)} = \delta_n^{(j)} \times \cos\beta, \tag{10}
$$

where β is the pitch helix angle of the rotor and $\delta_{n'}^{(j)}$ is the normal clearance distributed at end-section profile.

Moreover, in order to obtain the normal clearance $\delta_{n'}^{(j)}$, it is necessary to calculate the relevant normal direction. To simplify the calculation process, the ratio ε of the radial clearance $\delta_d^{(j)}$ to the normal clearance $\delta_{n'}^{(j)}$ is defined as follows:

$$
\begin{aligned}
\varepsilon^{(j)} &= \frac{\left(p\left(\partial y_{1,j}/\partial u\right)\right)^2+\left(-p\left(\partial x_{1,j}/\partial u\right)\right)^2+\left(x_{1,j}\left(\partial x_{1,j}/\partial u\right)+y_{1,j}\left(\partial y_{1,j}/\partial u\right)\right)^2}{\left(p\left(\partial y_{1,j}/\partial u\right)\right)^2+\left(-p\left(\partial x_{1,j}/\partial u\right)\right)^2}, \quad j=1,2,\ldots,\\
\delta_d^{(j)} &= \delta_{n'}^{(j)} \times \varepsilon^{(j)}.
\end{aligned}
\tag{11}
$$

In this paper, the meshing clearance is arranged based on the clearances distributed at some special positions, such as tooth top, tooth root, node point, and pendulum point. These positions are located near the top circle or the root circle of the rotor, as shown in Figure 3(d). According to the characteristics of the end-section profile, radial and normal directions of these positions coincide basically, namely, $\varepsilon \approx 1$. Hence, by calculating the radial clearance, the complex calculation of the normal clearance is simplified.

3.2. The Meshing Clearance Calculation Procedure. The correct estimation of meshing clearance directly impacts on the efficiency and performance of twin-screw compressors. Rotor clearance is mainly affected by temper-

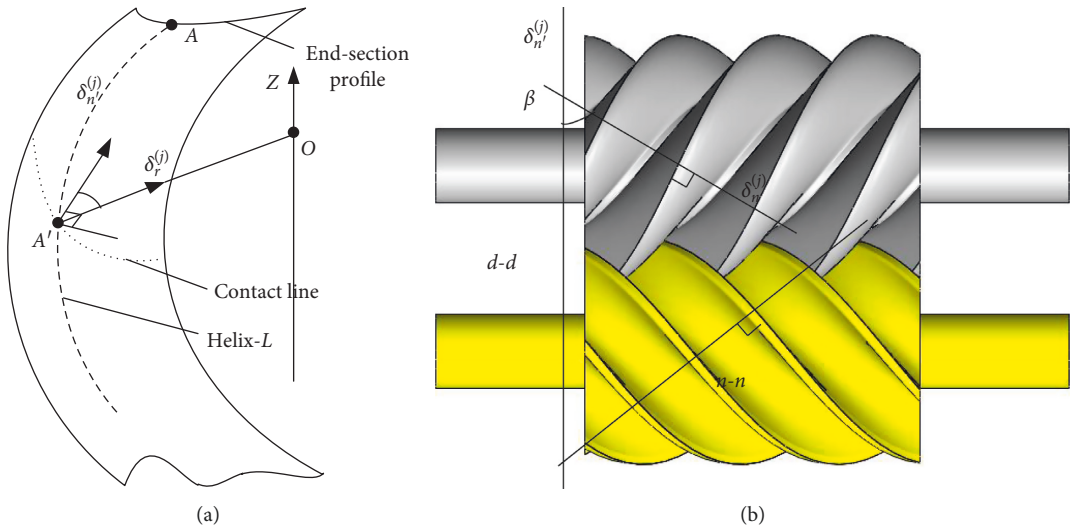

Figure 2: Schematic diagram of meshing clearance: (a) ratio between radial clearance and normal clearance of end-section; (b) normal clearance ratio between end-section and normal-section profile.

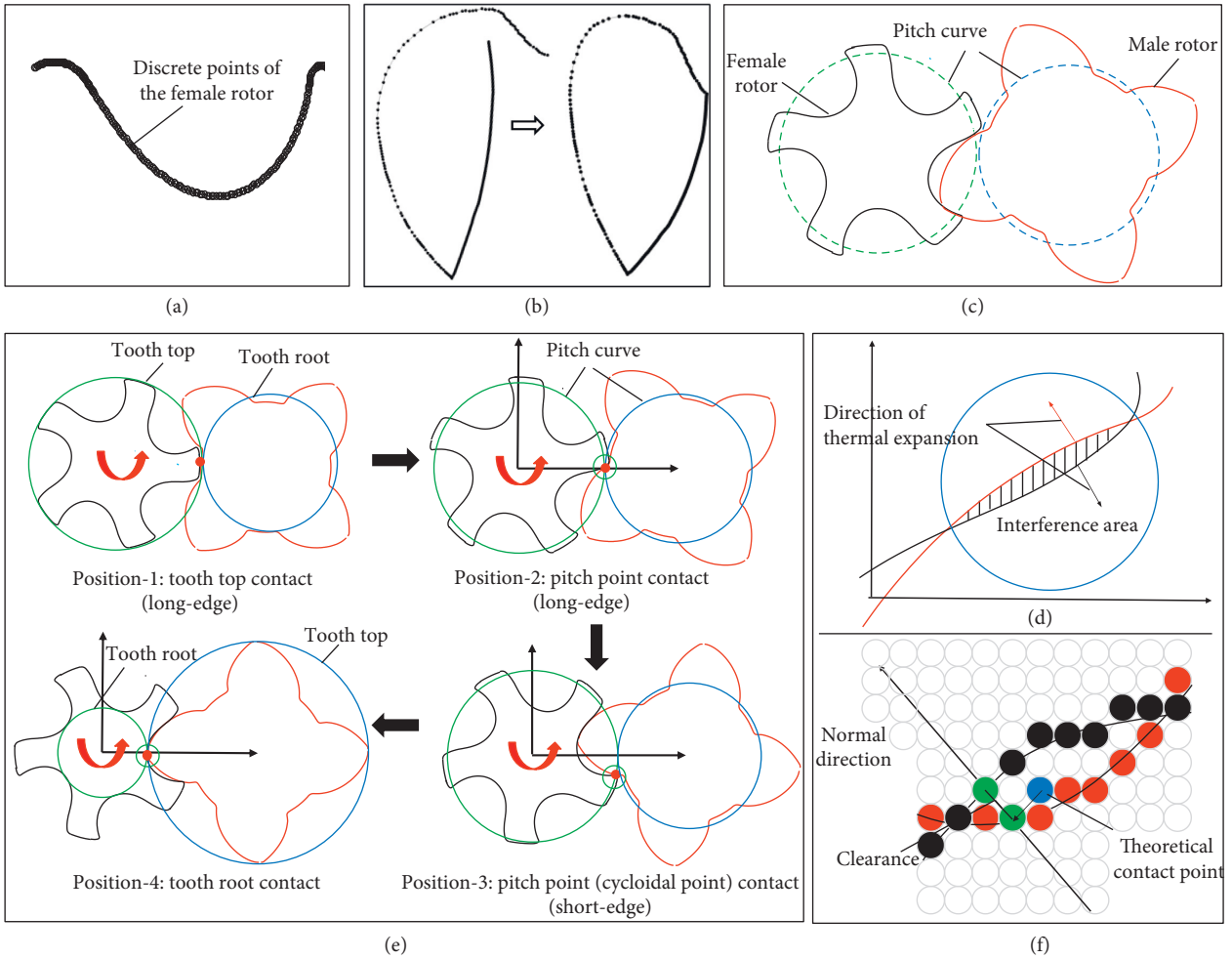

Figure 3: Main program descriptions for meshing clearance calculation: (a) female rotor profile, (b) 3D contact line, (c) screw rotor pair, (d) rotor profiles after thermal deformation, (e) instantaneous contact model, and (f) meshing clearance calculation.

ature, pressure, and other factors. Different temperature and pressure conditions will cause significant changes in the deformation of the rotor and shell. Therefore, according to 2D measuring data points from the end-section profile of a female rotor and considering the thermal deformation of the rotor, the meshing clearance is determined.

The main procedure is illustrated in Figure 4. Firstly, as shown in Figure 3(a), the data points of the female rotor profile and the required geometric parameters are imported into the developed program. The enveloping equation is established, and then the dichotomy described in Section 2 is used to determine the discrete contact points, as shown in Figure 3(b). Combined with the coordinate transformation, the cubic spline fitting method described in Section 2 is then used to determine the curves for the male and female rotors, as shown in Figure 3(c). Considering the thermal deformation of the rotor pair during the working process, the interference region between the end-section profiles can be obtained, as shown in Figure 3(d). Relying on the relative motion between the rotor pair, the theoretical contact point at some special meshing positions (tooth top, tooth root, node point, and pendulum point) can be specified. According to the step-u, corresponding to these meshing points, the related profile points (x_1', y_1') from the actual profile (i.e., profile after thermal deformation) of the female rotor are obtained. Then, the instantaneous contact model at these positions can be established, as shown in Figure 3(e). For calculating the meshing clearance quickly and accurately, the coordinates of the interference region after thermal deformation are transformed into pixel coordinates. Subsequently, by calculating the minimum distance between the profile point (x_1', y_1') and the intersection point (intersection point of the normal vector of point (x_1', y_1') and the actual profile of the male rotor), the normal clearance can be obtained, as shown in Figure 3(f).

To realize the conversion between theoretical coordinates and pixel coordinates of the male and female rotors, it is assumed that the actual end-section profile coordinates of the two rotors are $\mathbf{r}_i'(x_i', y_i')$, $i = 1, 2$, and the minimum distance between the two adjacent points on end-section profiles is d. The coordinate origin after conversion to the pixel coordinate system can be expressed as (x_{i0}', y_{i0}'). Then, the transformation equation can be obtained as

$$\mathbf{r}_{pi}' = \left[x_{pi}', y_{pi}'\right] = \left[\left\lceil \frac{\mathbf{r}_i'}{d} \right\rceil - \mathbf{r}_{i0}' = \left[\left\lceil \frac{x_i'}{d} \right\rceil - x_{i0}', \left\lceil \frac{y_i'}{d} \right\rceil - y_{i0}'\right], \quad i = 1, 2. \tag{12}$$

To obtain the actual profiles of the two rotors after thermal deformation, a temperature sensor is used to measure the exhaust and intake temperature. After some repeated experiments, the average temperature of the exhaust and intake could be obtained.

Combining with the finite element simulation technology, the maximum radial expansion ratio of the rotor is obtained. When the theoretical distance from each of profile points to the rotor center is given, the new coordinates of the profile points are obtained by multiplying the expansion ratio. The interference phenomenon between the two rotor profiles is presented due to the influence of thermal expansion, and the interference value is the main factor, which determines the meshing clearance. The deformation trend of the male and female rotor profiles affected by thermal deformation is shown in Figure 3(d), and the arrow direction indicates the normal direction of thermal deformation.

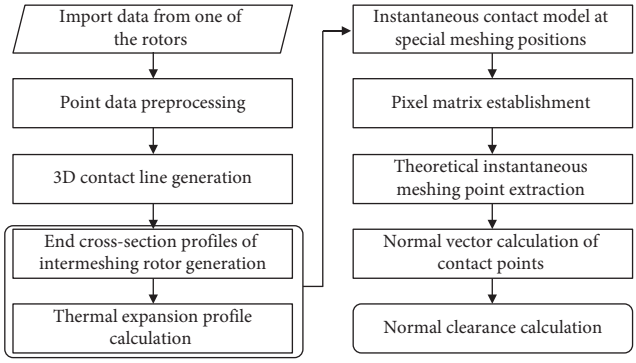

Figure 4: Overall flow chart for the study.

According to the instantaneous contact model at the special positions, as shown in Figure 3(e), the actual profile of the male rotor is swept along the normal direction of the actual profile point (x_1', y_1'), and the intersection point between the actual profile and the normal line is obtained. Then, the meshing clearance between the two rotors is extracted. To do this, according to the step-u, corresponding to the special meshing points on the theoretical profile of the female rotor, the corresponding actual profile point (x_1', y_1') is obtained. Then, the coordinates of this point are transformed into a pixel coordinate (x_{p1}', y_{p1}') by equation (12). The cumulative chord length cubic parameter splines are used to interpolate the actual profile of the female rotor. The derivatives of the discrete points versus the cumulative chord lengths s are calculated and recorded as $((\partial x_{p1}'/\partial s), (\partial y_{p1}'/\partial s))$. Then, the normal equation of the pixel (x_{p1}', y_{p1}'), belonging to the actual profile of the female rotor, is as follows:

$$\left|\frac{\partial y_{p1}'}{\partial s} y + \frac{\partial x_{p1}'}{\partial s} x - \frac{\partial y_{p1}'}{\partial s} y_{p1}' - \frac{\partial x_{p1}'}{\partial s} x_{p1}'\right| < \eta, \tag{13}$$

where η is a certain error range. Equation (12) shows that the pixels are all integers; thus, errors must occur in the process of coordinate transformation. Therefore, when the above condition is satisfied, the normal line equation of the pixel (x_{p1}', y_{p1}') can be established.

Since the female rotor is used as the scan benchmark, the normal direction of the pixel (x_{p1}', y_{p1}') should be opposite to the expansion direction of the female rotor. It is assumed that η is the angle between the line formed from the origin center of the female rotor to the pixel (x_{p1}', y_{p1}'), and the positive direction is the same with y-axis. When the pixel coordinates (x, y) at any point are substituted in equation (14) and after satisfying the following condition, the normal direction can be confirmed.

$$f = x\cos\eta + y\sin\eta - x_{p1}'\cos\eta - y_{p1}'\sin\eta < 0. \tag{14}$$

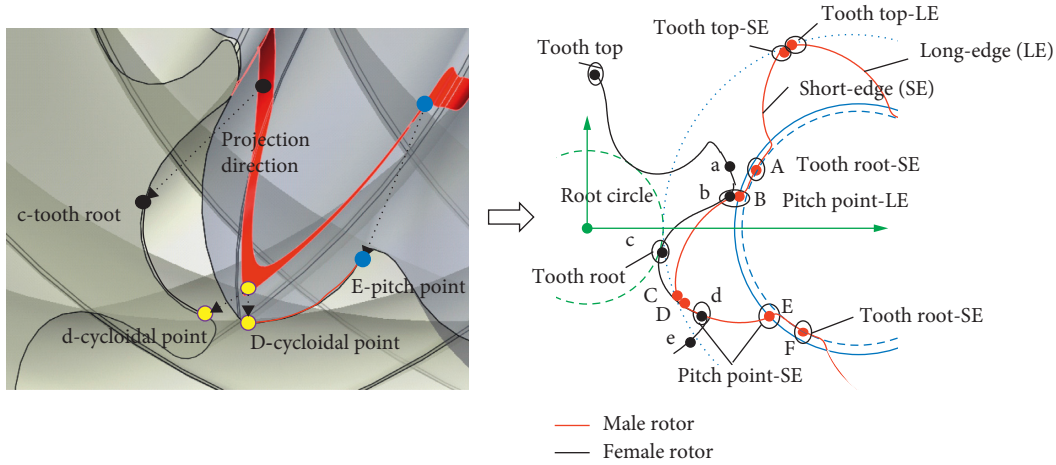

Figure 5: End profiles and 3D meshing line of the rotor pair.

Table 1: Curves forming the end-section profile.

End-section profile	Curve properties	Conjugate curve	Properties of conjugate curve
AB	Arc	ab	Arc
BC	Archimedes line	bc	Envelope of archimedes line
D	Cycloidal point	cd	Cycloidal segment
DE	Cycloidal segment	d	Cycloidal point
EF	Arc	de	Arc
FA	Arc	ea	Arc

When the pixel coordinates (x'_{p1}, y'_{p1}) from the actual profile of female rotor are substituted in equation (13), the corresponding normal line can be obtained. By the principle of normal direction judgment in equation (14), all pixels $\left\{(x_{p2}^{(m)'}, y_{p2}^{(m)'}) \,|\, m = 1, 2, \ldots\right\}$ from the actual profile of the male rotor near this line can be scanned. Since pixels are all integers, there may be several nearest pixels. In order to obtain an accurate meshing clearance, it is necessary to restore all the obtained pixels to the theoretical coordinate system for judgment. By solving the distance between the theoretical points $\left\{(x_2^{(m)'}, y_2^{(m)'}) \,|\, m = 1, 2, \ldots\right\}$ and the contact point (x'_1, y'_1), the minimum distance is extracted and defined as meshing clearance:

$$l = \min\left\{ l_m \,\middle|\, l_m = \sqrt{\left(x'_1 - x_2^{(m)'}\right)^2 + \left(y'_1 - y_2^{(m)'}\right)^2} \right\}, \quad m = 1, 2, \ldots. \tag{15}$$

4. Overview of the Meshing Clearance Layout Procedure

Figure 5 shows the end-section profiles and 3D meshing line of twin-screw rotors. Table 1 shows the curves forming the end-section profile. To confirm that the meshing clearance is uniformly distributed on the contact line, a meshing clearance layout method is proposed.

(1) *Arrange the Top Clearance between the Rotor Cylindrical Surface and the Shell.* According to the size of the shell, the outer diameter of the rotor should be adjusted first to ensure the clearance between the rotor and the shell, and the clearance should be as small as possible.

Table 2: Geometrical parameters and operating conditions for the compressor.

Items (units)	Values
Tooth number	4 (male)/6 (female)
Assembly center distance (mm)	100.04
Pitch helix angle (degree)	44.4
Outer diameters (mm)	140 (male)/122 (female)
Rotor material/expansion rate	$45\#/1.25 \times 10^{-5}$
Operating rotation speed (rpm)	2960
Exhaust volume (m^3/min)	6
Exhaust temperature degree (°C)	71
Rotor surface temperatures (°C)	200

(2) *Arrange the Clearance between the Cycloidal Point-d of the Female Rotor and the Corresponding Cycloidal Segment-DE of the Male Rotor.* To prevent the wear of cycloidal point on the short-edge of the female rotor, the top point of the short-edge is usually designed as an arc. From the instantaneous meshing line, the pitch circle of the female rotor generally intersects the arc. Therefore, the pitch points on the short-edge are generally regarded as cycloidal point. According to the conjugate principle of the rotor profile, there is a cycloidal point (i.e., pitch point) on the short-edge of the female rotor, meshing with the short-edge profile segment from the tooth top to the pitch point of the male rotor. If the clearance is arranged not on

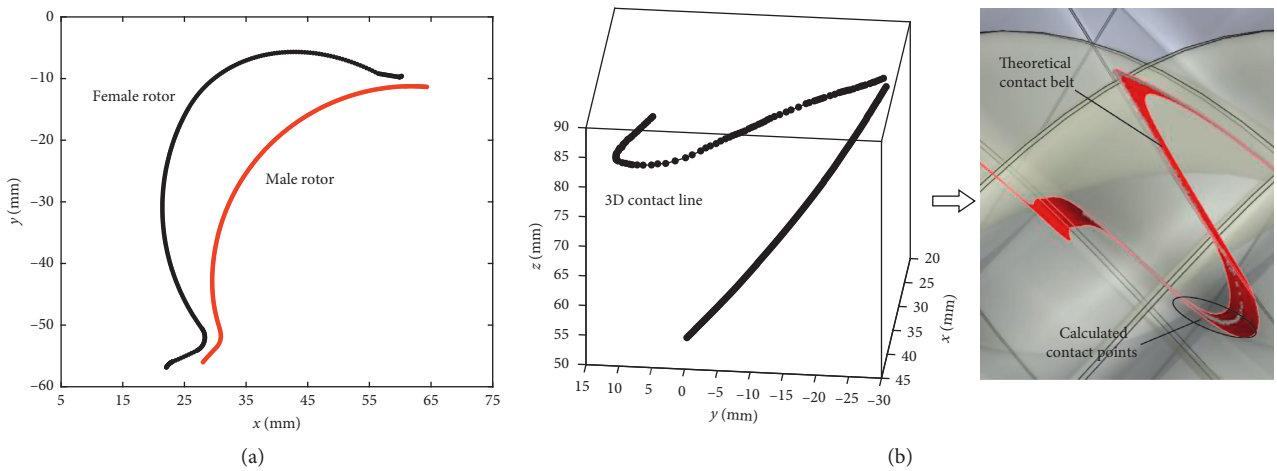

Figure 6: Solution of the rotor pair: (a) rotor profile; (b) 3D contact line.

the male rotor profile but only on the cycloidal point of the female rotor profile, the equal clearance values are uniformly distributed on this contact band, and the clearance cannot be minimized at the pitch point. Therefore, it is necessary to adjust the clearance on the cycloid section of the male rotor. A variable clearance band is arranged to maximize the clearance at the tooth top and to minimize the clearance at the pitch circle of the rotor.

(3) *Arrange the Clearance between the Cycloidal Point-D of the Male Rotor and the Cycloidal Segment-cd of the Female Rotor*. For the male rotor profile, the top point of the short-edge is usually defined as the cycloidal point, meshing with the short-edge profile segment from the pitch point to the tooth root of the female rotor. It should be noted that the cycloidal points on the long and short edges of the male rotor coincide theoretically. However, to prevent the wear of cycloidal point, excessive arcs are generally designed between the cycloid points on long and short edges. Similarly, the clearance should be arranged on the cycloidal segment of the female rotor.

(4) *Arrange the Tooth Root Clearance of the Female Rotor*. Since the meshing clearance between the cycloidal point (i.e., pitch point) of the female rotor and the cycloidal segment of the male rotor has been arranged, the clearance at the pitch circle of the female rotor profile can be determined. Therefore, the tooth root clearance of the female rotor can be determined only on the basis of the requirement of the tooth root clearance.

(5) *Arrange the Clearance between the Long-edge Segments of the Male and Female Rotors*. Since the long-edge segments of the two rotors engage through point contact, it only needs to adjust the pitch point and the tooth root coordinates on the male and female rotors.

(6) *Clearance Distribution along 3D Contact Line*. Through the above arrangements, the meshing clearance distributed on the end-section profiles can be identified. When the meshing clearance of the end-section profiles at each point is substituted in equation (10) and when the corresponding normal vector is obtained by equation (2), the corresponding point coordinate $\mathbf{r}_{c'}^{(j)}$ of 3D contact line can be obtained.

Table 3: Clearance layout requirements of SIERRA-SL37 rotors.

Items (units)	Values
Root clearance (mm)	0.22
Clearance of pitch point (mm)	0.17
Top clearance of the male rotor long edge (mm)	0.21
Top clearance of the male rotor short edge (mm)	0.19

5. Numerical Example

5.1. Solution of Theoretical Profile and Contact Line. In order to validate the meshing clearance layout method established in this paper, the SIERRA-SL37 dry twin-screw compressor offered by Ingersoll Rand is used to calculate the meshing clearance for the rotor pair. The sampled female rotor is generally measured to determine the end-section profile. The rotor parameters and the other operating parameters for the compressor are listed in Table 2.

Since the end-section profile of the female rotor is known, the profile of the male rotor is enveloped according to the profile of the female rotor, as shown in Figure 6(a). Combined with equation (5), the contact line is shown in Figure 6(b). The spatial curve composed of grey points is the instantaneous contact line, and the red part is the contact band of the two rotors. From this figure, the solved contact line falls in the contact band, which verifies the correctness of the theory.

5.2. Meshing Clearance Layout. The increase of rotor temperature will result in the change of operational clearances. The test condition, with a surface temperature of 200°C, is simulated in the rotor model to determine how the thermal

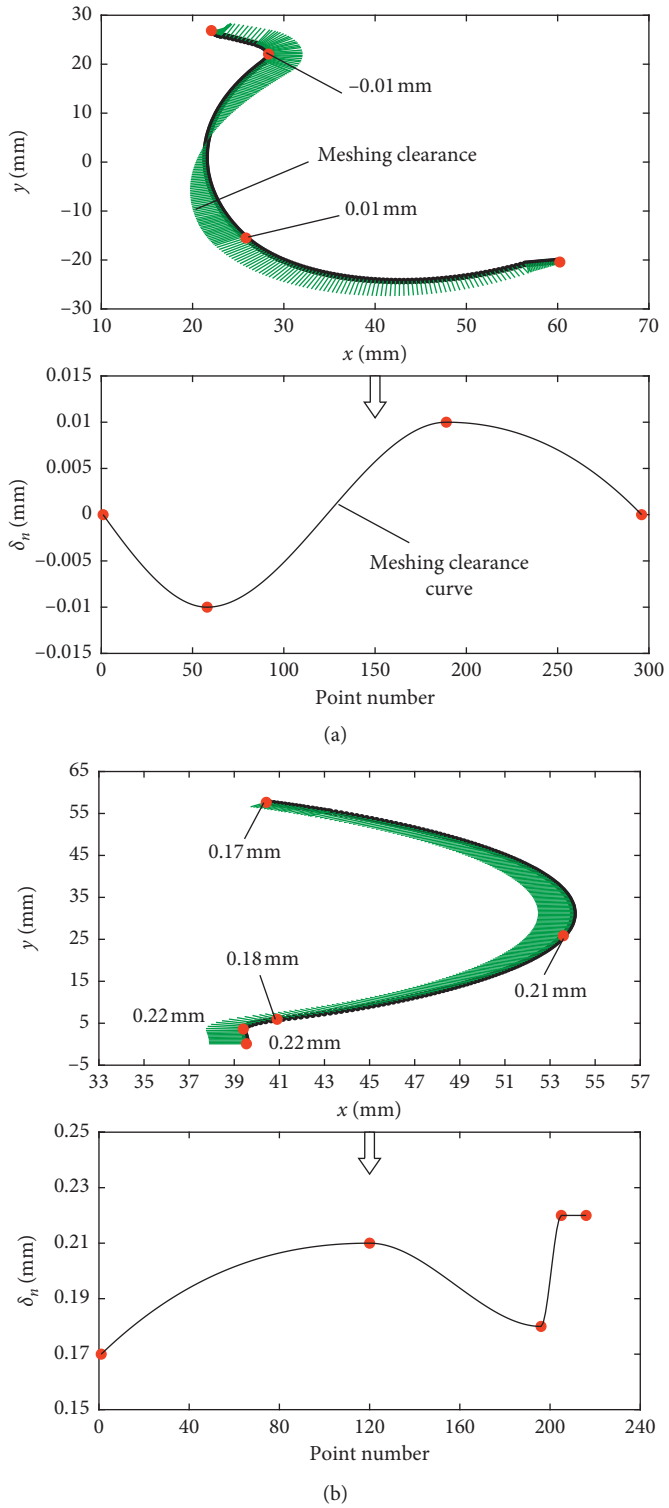

Figure 7: Meshing clearance for MCL: (a) meshing clearance of female rotor; (b) meshing clearance of male rotor.

deformation varied throughout the compression cycle. Through finite element simulation analysis, the maximum radial expansion ratio of the rotor is 0.0067175. By multiplying the distance from each profile point to the center of the rotor with the expansion ratio, the new rotor profile coordinates can be obtained.

The instantaneous contact models, considering the thermal deformation, are established. The thermal deformation at each special meshing position can be calculated by using the engagement-pixel tracking (EPT) technique. For the end-section profile of the female rotor, the tooth top deformation of the long edge is 0.14 mm and that of the pitch

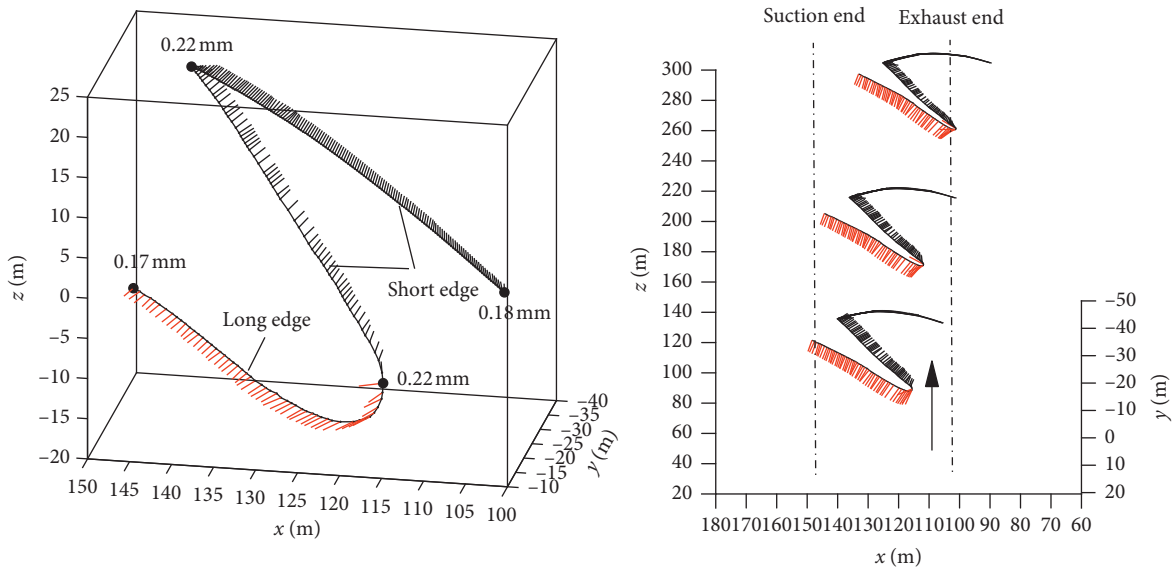

Figure 8: Variation of the meshing clearance with the rotational angle of rotor.

Table 4: State parameters of the compressors.

Exhaust volume (m^3/min)	Air supply pressure (MPa)	Exhaust temperature (°C)
6	0.84	71
12	0.80	56
22	0.98	78

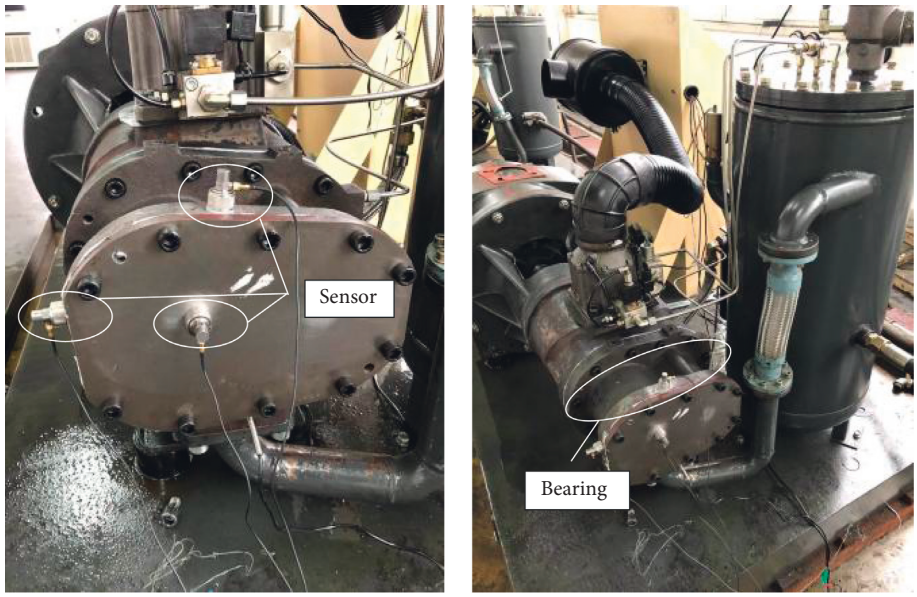

Figure 9: Experimental platform of twin-screw compressor.

point is 0.08 mm, while the corresponding deformation at these two positions of the short-edge are 0.1 mm and 0.09 mm, respectively. The deformation of the tooth root is 0.01 mm, and the pore diameter of the shell is 120.28 mm. For the end-section profile of the male rotor, the tooth top deformation of the long edge is 0.19 mm and that of the pitch point is 0.09 mm, while the corresponding deformation at these two positions of the short-edge are 0.21 mm and 0.08 mm, respectively. The deformation of the tooth root is 0.08 mm, and the pore diameter of the shell is 140.38 mm. Finally, based on these results, Table 3 shows the clearance layout requirements of SIERRA-SL37 rotors.

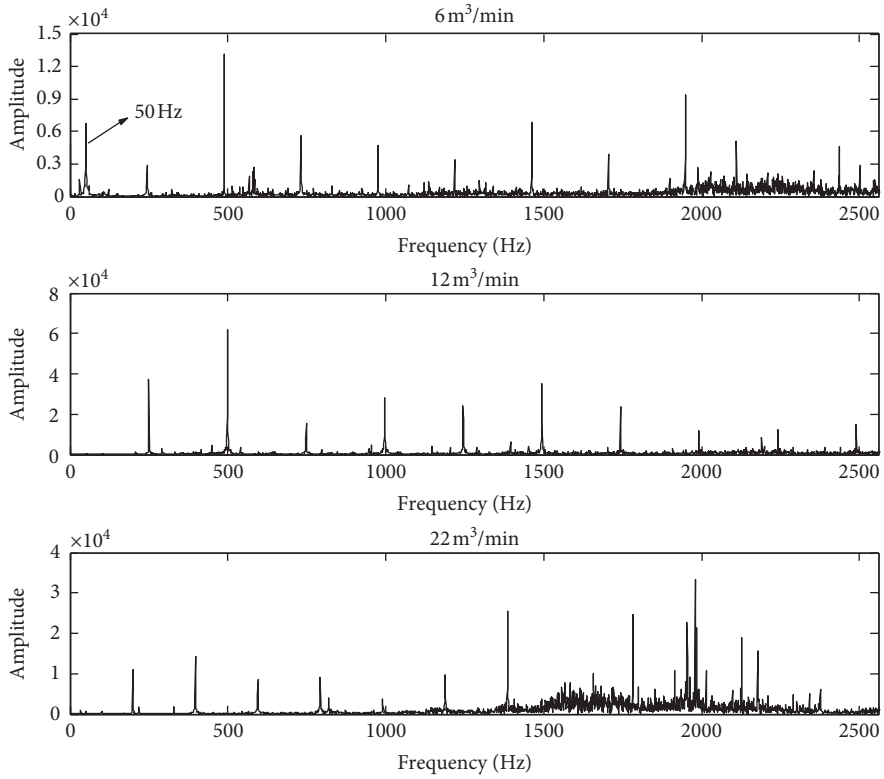

Figure 10: Frequency-domain curves of compressors operation.

According to clearance arrangement requirements:

(1) For the end-section profile of the male rotor, the normal adjustment of 0.21 mm is arranged at the top circle of the long edge and 0.19 mm is arranged at the top circle of the short edge. Since the requirement of the root clearance is 0.22 mm, the normal adjustment of 0.01 mm should be arranged at the root circle of the female rotor.

(2) For the end-section profile of the female rotor, to ensure the uniform variation of the clearance from the tooth root to the cycloidal point (i.e., pitch point) of short-edge, the normal adjustment of −0.01 mm is arranged at the cycloidal point of the short-edge, and the normal clearance variation formed by the tooth top of the male rotor is 0.02 mm. At this time, in order to ensure the clearance of 0.17 mm at pitch point of the short-edge, the normal adjustment of 0.18 mm is arranged at the pitch point of the male rotor short-edge.

(3) Since the top circle of the female rotor is taken as the reference, the top circle of the female rotor is not adjusted. To ensure the root clearance of the male rotor is 0.22 mm, the normal adjustment of 0.22 mm is arranged at the tooth root of the male rotor. To meet the requirement of clearance arrangement at the pitch point of long edge, a normal adjustment of 0.17 mm is arranged at the pitch point of the male rotor long edge, while no normal adjustment is arranged at the long-edge segment from the tooth root to the tooth top of the female rotor. The clearance distributed on end-section profiles of the male and female rotors is shown in Figure 7.

Table 5: Characteristic frequency.

Exhaust volume (m^3/min)	6	12	22
Frequency (Hz)	244	249	199
	488	498	398
	732	747	597
	976	996	796
	1220	1245	995
	1464	1494	1194

5.3. Clearance Distribution along 3D Contact Line. When the meshing clearance and the normal vector at each point are substituted in equation (10), the corresponding 3D contact line point coordinate $\mathbf{r}_{c_i}^{(j)}$ can be obtained, as shown in Figure 8. The variation of meshing clearance may provide a more practical data support for leakage analysis and volumetric efficiency of compressors [18].

5.4. Performance Predictions. The screw compressor runs at the nominal air test environment, which is closest to the designed simulation conditions, with a speed of 2960 r/min and an exhaust volume of 6/12/22 $m^3 \cdot min^{-1}$. Table 4 shows the state parameters of the compressors. To examine the reliability of the compressors after clearance arrangement, the time-domain curves of vibration for the compressors were collected by vibration measuring equipment, and the

frequency-domain curves of the compressor operations are obtained by FFT. The vibration characteristics for different exhaust volumes of the compressors were analyzed, and the reliability of clearance arrangement for the rotors was also verified by judging the operation status of different compressors.

In the process of data acquisition, the magnetic seats with installation thread are fixed to the bearing house of the compressor. The data at each measurement point from three directions, the x-axis (horizontal radial), the y-axis (vertical), and the z-axis (horizontal axis), are collected, as shown in Figure 9. The evaluate standard of compressor vibration state is analyzed by frequency spectrum.

As shown in Figure 10, the spectrum of the vibration signal shows a clear multiple spectrum peak within the valid frequency range of sampling data. This shows that good meshing quality of the rotor pair is acquired, and there are no contact impact problems. If the clearance arrangement is unreasonable, the meshing impact of the rotor pair will be strengthened, and the excitation frequency is the meshing frequency. The above experimental results validate the rationality of clearance arrangement.

As shown in Figure 10, the peak frequency of the spectrum appears at 50 Hz. For this, the characteristic frequencies of these three compressors are shown in Table 5. The spectrum peaks of the amplitude in the x directions show good linear law. There are no multifrequency peaks at this frequency, which shows that it is the disturbed frequency. More detailed analyses indicated that the signal is disturbed by alternating current (50 Hz) due to the installation errors.

6. Conclusion

Previous studies on meshing clearance simulation are mainly based on theoretical profiles, which are obtained by the tooth profile equation. However, actual profiles are affected by manufacturing, assembly variation, and thermal expansion. Therefore, due to unknown rotor profile of the screw compressor, in this paper, the profile is given in the form of discrete data collected by the measuring system. With the piecewise cubic spline interpolation, the 3D contact line and the theoretical contact points at some special meshing positions can be obtained. In addition, an EPT algorithm is proposed to evaluate the clearance along the 3D contact line. The clearance value of the 3D contact line can be obtained by projecting the meshing clearance of the end-section onto the normal section, which simplified the previous calculation method. The proposed method can ensure the uniform change of the clearance on the whole 3D contact line. Actual time-domain curves of vibration for the compressors demonstrate the accuracy of the proposed algorithm as well. The proposed method can be used as a tool for evaluating the clearance distribution of actual machined profiles.

Data Availability

The data used to support the findings of this study have not been made available because the data are obtained from confidential data of products.

Conflicts of Interest

The authors declare that there are no conflicts of interest regarding the publication of this paper.

Acknowledgments

This work was funded by the Project of China Postdoctoral Science Foundation (no. 2019M652256).

References

[1] J. Sauls, G. Powell, and B. Weathers, "Thermal deformation effects on screw compressor rotor design," in *Proceedings of the International Conference on Compressors and Their Systems*, pp. 159–168, Chandos Publishing, London, UK, September 2007.

[2] Y. Zhao, S. Zhao, W. Wei, and H. Hou, "Precision grinding of screw rotors using CNC method," *International Journal of Advanced Manufacturing Technology*, vol. 89, no. 9–12, pp. 2967–2979, 2017.

[3] L. Tao, Y. Wang, Y. He et al., "A numerical method for evaluating effects of installation errors of grinding wheel on rotor profile in screw rotor grinding," *Proceedings of the Institution of Mechanical Engineers Part B Journal of Engineering Manufacture*, vol. 230, no. 8, pp. 1381–1398, 2016.

[4] J. Willie and R. Sachs, "Structural and torsional vibration and noise analysis of a dry screw compressor," *Proceedings of the Institution of Mechanical Engineers, Part E: Journal of Process Mechanical Engineering*, vol. 231, no. 1, pp. 4–13, 2017.

[5] D. Yan, Q. Tang, A. Kovacevic, S. Rane, and L. Pei, "Rotor profile design and numerical analysis of 2-3 type multiphase twin-screw pumps," *Proceedings of the Institution of Mechanical Engineers, Part E: Journal of Process Mechanical Engineering*, vol. 232, no. 2, pp. 186–202, 2018.

[6] S. V. Erdeweghe, J. D. Schutter, and E. V. Bulck, "Integral modeling of a twin-screw compressor," *Journal of Mechanical Design*, vol. 138, no. 7, Article ID 073401, 2016.

[7] Z. Shen, B. Yao, W. Teng, W. Feng, and W. Sun, "Generating grinding profile between screw rotor and forming tool by digital graphic scanning (DGS) method," *International Journal of Precision Engineering and Manufacturing*, vol. 17, no. 1, pp. 35–41, 2016.

[8] R. Huang, T. Li, X.-L. Yu, F.-L. Liu, and Q.-K. Feng, "An optimization of the star-wheel profile in a single screw compressor," *Proceedings of the Institution of Mechanical Engineers, Part A: Journal of Power and Energy*, vol. 229, no. 2, pp. 139–150, 2015.

[9] Z. W. Xing, *Screw Compressors: Theory, Design and Application*, China Machine Press, Beijing, China, 2000, in Chinese.

[10] Y. C. Huang, J. Y. Lai, F. Y. Lin, and Y. L. Guo, "Two-dimensional localisation and clearance evaluation of screw rotors," *International Journal of Computer Applications in Technology*, vol. 37, no. 1, p. 74, 2010.

[11] T. N. Mustafin, R. R. Yakupov, M. S. Khamidullin, I. G. Khisameev, L. H. Uybekova, and O. Y. Paranina, "Determining of actual profile clearances and screw compressor rotor positions depending on working conditions," *IOP Conference Series: Materials Science and Engineering*, vol. 232, p. 74, 2017.

[12] Y. R. Wu and J. W. Chi, "A numerical method for the evaluation of the meshing clearance for twin screw rotors with discrete tooth profile points," *Mechanism & Machine Theory*, vol. 70, no. 6, pp. 62–73, 2013.

[13] Y. L. Jiing, C. H. Yi, Y. L. Feng, and Y.-L. Guo, "Meshing simulation and clearance evaluation of real screw rotors," *Journal of the Chinese Institute of Engineers*, vol. 35, no. 7, pp. 887–900, 2012.

[14] D. Buckney, A. Kovacevic, and N. Stosic, "Design and evaluation of rotor clearances for oil-injected screw compressors," *Proceedings of the Institution of Mechanical Engineers Part E Journal of Process Mechanical Engineering*, vol. 231, no. 1, pp. 26–37, 2017.

[15] D. Buckney, A. Kovacevic, and N. Stosic, "Rotor clearance design and evaluation for an oil injected twin screw compressor," *IOP Conference Series: Materials Science and Engineering*, vol. 90, 2015.

[16] M. H. Jones and S. A. Velinsky, "Contact kinematics in the roller screw mechanism," *Journal of Mechanical Design*, vol. 135, no. 5, Article ID 051003, 2013.

[17] X. J. Fu, G. Liu, S. J. Ma, R. T. Tong, and T. C. Lim, "A comprehensive contact analysis of planetary roller screw mechanism," *Journal of Mechanical Design*, vol. 139, no. 1, Article ID 012302, 2017.

[18] B. R. Munson, D. F. Young, T. H. Okiishi et al., *Fundamentals of Fluid Mechanics*, John Wiley & Sons, Hoboken, NJ, USA, 2009.